Local structure of disordered $Bi_{0.5}K_{0.5}TiO_3$ investigated by pair distribution function analysis and first principles calculations

Bo Jiang, Tor Grande and Sverre M. Selbach*

Department of Materials Science and Engineering,
NTNU Norwegian University of Science and Technology, 7491 Trondheim, Norway.

*Correspondence should be addressed to selbach@ntnu.no

Abstract

We investigate A-site cation ordering in the ferroelectric perovskite $Bi_{0.5}K_{0.5}TiO_3$ (BKT) by Density Functional Theory (DFT) calculations and synchrotron X-ray total scattering. Using BKT as a prototypical lead-free ferroelectric perovskite with mixed A-site cations, we use a combination of theory and experiments to assess the energetics and resulting physical properties of cation ordering. Ten different Bi/K configurations in a 2×2×2 supercell were assessed by real space pair distribution functions (PDF) and DFT calculations. None of these configurations were identified as particularly favourable from experiment or theory. Ferroelectric polarization calculated by the Berry phase method for all ten configurations yield values of 50-105 $\mu C/cm^2$. This is significantly larger than previously reported experimental results in the range of 22-49 $\mu C/cm^2$, indicating that BKT does not possess long range A-site cation order. Reverse Monte Carlo (RMC) modelling of the total scattering data with a 12×12×12 supercell also supports substantial A-site disorder in BKT. A 4×4×4 supercell with local cation displacements in a pseudo-disordered A-site sublattice reproduces the experimentally observed polarization, implying that in a real material there are multiple local polar regions which partly cancel each other. The combination of RMC modelling of PDFs with DFT calculations should be highly applicable to other crystalline materials with sublattice disorder.

I. INTRODUCTION

Health, safety and environmental concerns call for the replacement of state-of-the-art lead containing piezoelectric and ferroelectric materials based on $Pb(Zr,Ti)O_3$ (PZT)[1, 2]. Bismuth is an attractive replacement for lead as the comparatively harmless Bi^{3+} cation also possesses a $6s^2$ lone electron pair like Pb^{2+}, inspiring efforts to develop Bi-based replacements for PZT[3-7]. $Bi_{0.5}Na_{0.5}TiO_3$ (BNT, rhombohedral *R*3*c*) with A-site disorder and related solid solutions have been widely studied due to its piezoelectric performance[8-11], whereas its analogue $Bi_{0.5}K_{0.5}TiO_3$ (BKT, *P*4*mm*, a = 3.933 Å, c=3.975 Å, c/a=1.01[12]) is less studied. BKT, first reported by Smolenskii et *al.* in 1961[13], and BKT-based solid solutions, are also promising ferroelectric piezoelectrics[14-16]. While single phase BKT can be prepared by conventional solid state synthesis[12, 17-19], challenges with sintering dense ceramics have hampered the study of pure BKT[17, 19]. Poling low density BKT ceramics is difficult due to the high coercive field[17] and the reported spontaneous polarization (P_s) varies between 22 and 49 $\mu C/cm^2$ [17, 20-25].

Early XRD analysis by Ivanova et *al.*[26] showed that BKT transforms from paraelectric cubic ($Pm\overline{3}m$) to a pseudo-cubic structure at a T_C of about 380 °C, and to ferroelectric tetragonal *P*4*mm* at the Burns temperature[27] T_D of about 270 °C. More recent work has reported T_C values of 370-410 °C and a T_D of 270-310 °C[1, 17, 19, 26, 28]. Relaxor behavior has been found in BKT with a broad dielectric peak with frequency dependent dielectric maximum temperature about 380°C.[4, 29] Solid solutions between BKT and ferroelectric rhombohedral *R*3*c* $BiFeO_3$ (BFO) display a morphotropic phase boundary (MPB) at about 60% $BiFeO_3$[30], and a pseudo-cubic phase with relaxor-like behaviour for 40-60% BFO[31, 32]. Optimal piezoelectric properties are found close to 25% BFO, with d_{33} = 250-370 pm/V in the temperature range of 25-175 °C.[33-35] Relaxor-like behavior has also been observed for all materials in $(1–x)$ $Bi_{0.5}K_{0.5}TiO_3–xBi_{0.5}Na_{0.5}ZrO_3$ (BKT-BNZ).[12]

Most piezoelectric materials are characterized by chemical and structural disorder, complicating the understanding of structure-property relationships, and hampering the prediction of new lead-free piezoelectrics. Cation ordering is known to have profound effects on the properties of ABO_3 perovskites, where A-site cations order less readily than B-site cations[36]. Electrostatic forces and a difference in the radius and formal charge of the cations on a mixed sublattice favours cation ordering[37], while configurational entropy and similarity of the cations in size and formal charge favours disorder. In contrast with the disordered material BNT[10, 11], where Bi^{3+} (1.31 Å) and Na^{+} (1.32 Å) have very similar ionic radii, the 21% larger K^{+} (1.65 Å) could provide a driving force for cation ordering. However, no superstructure peaks associated with cation ordering have been observed in BKT[37], and structural disorder has been inferred from previous investigations by Raman spectroscopy[4], XAFS[15] and TEM[16].

Here we report a local structure investigation of $Bi_{0.5}K_{0.5}TiO_3$ where we combine DFT calculations with pair distribution functions (PDF) obtained from synchrotron X-ray total scattering data. We show that no long-range A-site cation order is favourable in BKT, and combine Reverse Monte Carlo (RMC) simulations with DFT calculations to formulate a model for the inherently disordered structure of BKT. Unlike a conventional displacive ferroelectric, the macroscopic polarization of BKT can be understood as the sum of many local, but partly cancelling, polar regions.

II. EXPERIMENTAL AND COMPUTATIONAL DETAILS

$Bi_{0.5}K_{0.5}TiO_3$ powder was prepared by a conventional solid state synthesis route with dried Bi_2O_3 (99.9%; Aldrich, Steinheim, Germany), K_2CO_3 (99.99%; Aldrich) and TiO_2 (99.9%; Aldrich) as precursors. The reactants were first mixed in a mortar and then ball milled for 24h in isopropanol using 5 mm yttrium YSZ balls as described in ref. [12]. The powder mixture was dried, sieved, and calcined in air at 800 °C for 5 hours, with subsequent ball milling by the same

procedure as for the precursor mixture. After drying and sieving (250 μm) the powder was uniaxially pressed (100 MPa) to pellets followed by cold isostatic pressing (CIP) at about 200 MPa. The green body was immersed in sacrificial powder and sintered at 1060 °C for three hours. The crushed sintered pellets were sieved and annealed at 600°C for 12 h to relieve mechanical stresses introduced during crushing. $BiFeO_3$ powder as a reference material was prepared as previously reported.[38]

Synchrotron X-ray total scattering data of $Bi_{0.5}K_{0.5}TiO_3$ and $BiFeO_3$ powder samples were collected at room temperature at beamline ID22 (λ=0.199965Å) at the European Synchrotron Radiation Facility (ESRF) using a 2D plate detector (Perkin Elmer XRD 1611). Reciprocal space data was analyzed by Rietveld refinement using the General Structure Analysis System (GSAS)[39] program with the EXPGUI[40] graphical user interface. Pair distribution functions (PDF) were obtained with the PDFgetX3 software[41] using a Q_{max} of 22.8 $Å^{-1}$. Modelling of the G(r) was carried out with the PDFgui software[42] using the parameters obtained from the Rietveld refinements as starting parameters. Lattice constants, atomic positions and atomic displacement parameters (ADP) were refined in this work, using a *P*4*mm* model with Bi/K fixed at (0,0,0). Correlated atomic motion was modelled with a cutoff of 4 Å, details are given in the Supplementary Information. Reverse Monte Carlo (RMC) fitting of PDFs were performed with the RMCprofile software[43] using a 12×12×12 supercell containing 8640 atoms. The simulations ran for 24 hours on one 3.1GHz core CPU, generating 2.0×10^6 moves. The initial structure was obtained from Rietveld refinement with the *P*4*mm* structure, and the PDF G(r), the scattering function F(Q) and the X-ray Bragg peaks were fitted simultaneously. In the RMC simulations bond valence sum (BVS) restrictions were applied to avoid unphysical bond lengths, and Bi^{3+} and K^+ were allowed to swap places on the A sublattice.

Density functional theory (DFT) calculations were performed with the *Vienna Ab initio*

Simulation Package (VASP) code[44, 45] using the PBEsol functional[46, 47]. The spontaneous polarization P_s was calculated by the Berry phase method[48, 49]. The standard PBE projector-augmented wave (PAW)[45] potentials Bi_d ($5d^{10}6s^26p^3$), K_sv ($3s^23p^654s^1$) Ti_pv ($3p^63d^24s^2$) and O ($2s^2p^4$) supplied with VASP were used and plane waves were expanded up to a cutoff energy of 550 eV. Brillouin zone integration was done on a 3×3×3 gamma centered k-point grid for the 2×2×2 $Bi_{0.5}K_{0.5}TiO_3$ supercell with 40 atoms, and similar k-point densities were used for larger cells. The Hellman-Feynman forces on the ions were relaxed until they were below 0.001 eV/Å.

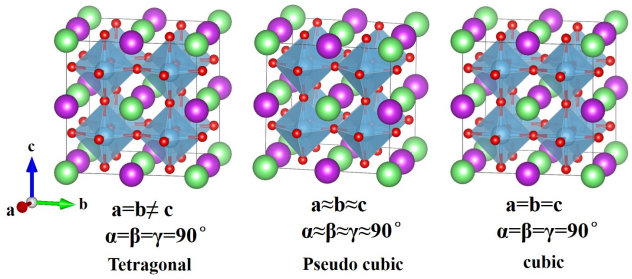

Figure 1: The 111 configurations of a 2×2×2 perovskite supercell of $Bi_{0.5}K_{0.5}TiO_3$ with tetragonal, pseudo-cubic and cubic lattice used in this work (Bi: purple, K: green).

Supercells containing 40 atoms represented by 2×2×2 perovskite unit cells were used in this work, as shown in Figure 1, where there are eight A-atoms situated on a simple cubic sublattice. "All the ordered configurations in this work are derived from the perovskite unit cell with tetragonal, pseudo-cubic and cubic lattice, corresponding to polymorphs with *P*4*mm*, pseudo-cubic and $Pm\overline{3}m$ symmetry found at different temperatures."

The pseudo-cubic structures have equal lattice vectors, but with the structural degree of freedom to allow displacements of ions from their centrosymmetric reference positions and small

deviations in the angles between the lattice vectors. For the 1:1 stoichiometric ratio of Bi and K in $Bi_{0.5}K_{0.5}TiO_3$, there are only six different configurations of A-atoms for cubic and pseudo-cubic structures, while there are ten different configurations possible for the lower symmetry tetragonal structures. All the configurations are shown in Figure 2 and named according to crystallographic directions as reported by Gröting and Albe[10, 11]. We note that the symmetry of these structures is lower than the labels we have chosen due to the inherent long range ordering of the two different cations on the A-site sublattice, and the space groups for ordered tetragonal structures are summarized in Table 1.

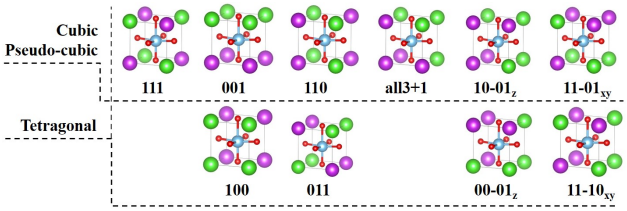

Figure 2: The 2×2×2 perovskite subunit supercell configurations of $Bi_{0.5}K_{0.5}TiO_3$. The simple cubic sublattice of A-atoms is shown with Bi as purple and K as green spheres, respectively. For a 1:1 Bi:K composition there are six configurations of A-sites for cubic and pseudo-cubic structures, and four additional configurations for the lower symmetry tetragonal structures.

III. RESULTS AND DISCUSSION

A. DFT analysis

We start our analysis by calculating the total energies of the different Bi/K-ordering schemes for the tetragonal, pseudo-cubic and cubic structures shown in Figures 1-2. The total energy was calculated for the ideal structures, after relaxing the ionic positions, and finally with full optimization of both ionic positions and lattice parameters, as summarized in Figure 3 and Table

1. Here, the zero energy level is set as the energy of the ideal 001 order for the tetragonal structure in Figure 3b as this configuration has the highest energy per formula unit of $Bi_{0.5}K_{0.5}TiO_3$. The energy gain compared to the ideal 001 tetragonal structure stems mostly from ionic relaxation, with small or negligible contribution from volume relaxation. In the case of the ideal cubic perovskite structure, the 110 ordering is the most favoured, while the 001 ordering has the highest energy. With fully optimized geometry, the 100, 011 and $10\text{-}01_z$ configurations are effectively degenerate and the three most energetically favoured, while the layered 001 configuration is the least stable. In the paraelectric ideal cubic structure Figure 3a the $10\text{-}01_z$ configuration is the most stable, while the rock salt-ordered 111 configuration is the least.

The six configurations within the cubic structure have higher energies than all the configurations in the ferroelectric tetragonal structure, except the 001. This is in accordance with BKT being ferroelectric *P*4*mm* at ambient and low temperatures, as found experimentally [26]. BKT transforms from ideal cubic $Pm\overline{3}m$ to a pseudo-cubic phase at T_D and to simulate this phase the lattice vectors are restricted to be equal, while the lattice angles and the ionic positions were relaxed. Here the energy gain relative to the ideal cubic structure stems predominantly from ionic relaxations with small or negligible contributions from volume relaxation, as also observed for the configurations within the tetragonal structure. For the pseudo-cubic structure the 001, 110 and $10\text{-}01_z$ configurations are effectively degenerate and the most stable, with very similar total energies to the three configurations favoured in the tetragonal structure. Hence, no single configuration of Bi^{3+} and K^+ can be identified as the most stable form 0K DFT calculations, indicating that BKT will be disordered at all temperatures as configurational entropy at finite temperatures will favour disorder. Although the lack of an enthalpic driving force for A-site cation ordering in BKT may be counterintuitive due to difference in size and formal charge of K^+ and Bi^{3+}, BKT does not possess any of the combinations of structural and

chemical features known to induce A-site cation ordering in perovskites[36]. Local non-stoichiometry, e.g. a local excess of Bi or K, is an additional possible source of structural disorder which we do not assess here as the different cell stoichiometry and charge compensation by electrons, holes or a background jellium charge precludes a direct comparison of the total energy of stoichiometric and non-stoichiometric local configurations.

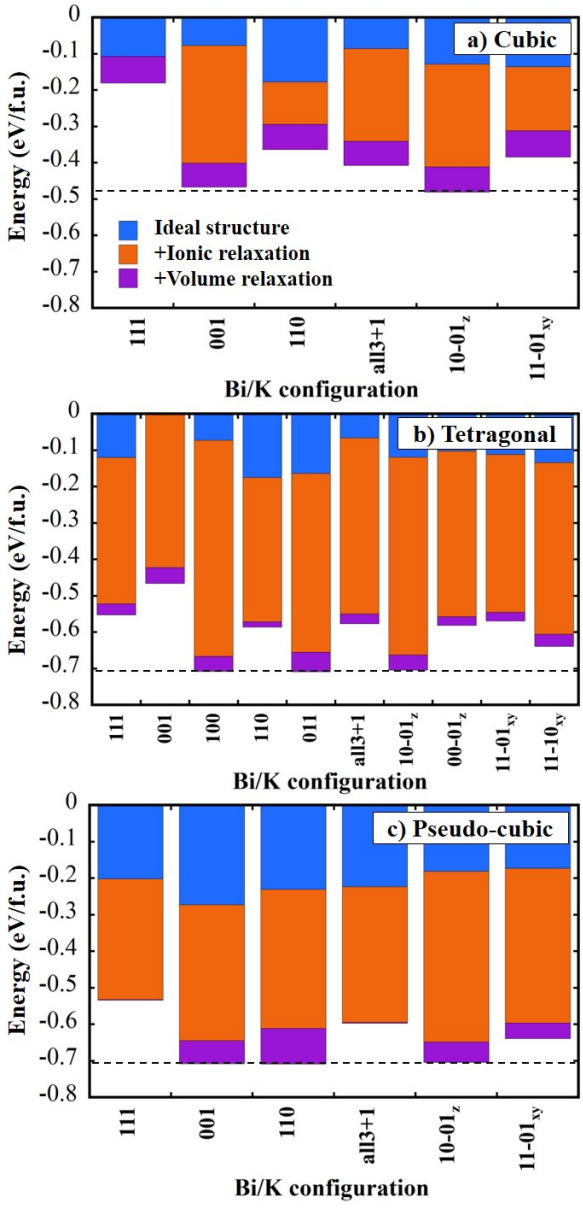

Figure 3: Relative energy per formula unit of the investigated A-site configurations in $Bi_{0.5}K_{0.5}TiO_3$ for (a) cubic, (b) tetragonal and (c) pseudo-cubic structures. The relative energy of the ideal structure without relaxation is shown in blue, the energy gain from ionic relaxation

in orange, and the additional energy gain from full geometry optimization in purple. The zero energy level is set as the energy of the ideal 001 structure with tetragonal lattice, which has the highest energy per formula unit.

Table 1. A-site configurations in 2×2×2 supercells of $Bi_{0.5}K_{0.5}TiO_3$ shown in Figure 2 with corresponding space groups, agreement factor R_w at low r range (1.5Å -6Å) from small-box fitting of experimental PDF, and DFT calculated Born effective charges (Z_{zz}) for the fully relaxed structures.

A-site configuration	Space group	R_w	Born effective charge for BKT (Z_{zz})		
			Bi^{3+}	K^+	Ti^{4+}
111	*I*4*mm*	0.54	3.93	1.18	4.95
Layer-001	*P*4*mm*	0.48	4.08	1.44	7.53
Layer-100	*Pmm*2	0.35	4.25	1.21	4.84
Columnar-110	*P*4*mm*	0.50	4.26	1.16	5.25
Columnar-011	*Amm*2	0.41	3.92	1.31	4.90
all3+1	*P*4*mm*	0.34	3.96-4.26	0.97-1.37	5.07-5.29
$10\text{-}01_z$	$P4_2mc$	0.32	3.96-4.24	1.21-1.29	4.88
$00\text{-}01_z$	*Pmm*2	0.45	3.87-4.56	1.04-1.38	5.43-5.54
$11\text{-}01_{xy}$	*P*4*mm*	0.39	3.61-3.96	1.04-1.47	5.17-5.20
$11\text{-}10_{xy}$	*Pmm*2	0.42	3.90-4.29	1.11-1.25	4.82-5.07
Exp	*P*4*mm*	0.36	5.37	1.07	7.42

For clarity, we have summarized the total energies of the fully relaxed structures in Figure 4a where the structures are grouped according to their A-site cation configuration. Only the most stable of the similar configurations 001/100, 110/011 and $11\text{-}01_{xy}$/$11\text{-}10_{xy}$ with tetragonal structure are shown in Figure 4a, and the horizontal dashed lines are guides to the eye. The fully optimized tetragonal and pseudo-cubic configurations of similar energies relaxed to equivalent structures with different polar axes. The unit cell tetragonality c/a of the fully relaxed

configurations with tetragonal structure shown in Figure 4b deviates strongly from the experimental value which is shown as a horizontal dashed line. All configurations except the 001 show larger c/a ratios than the experimental value of 1.01[12]. This indicates that the experimentally observed c/a ratio is the spatial average of a large number of local regions with lattice strain in different crystallographic directions, which again is governed by the local A-site cation configuration. In perovskites with tetragonal structure the spontaneous polarization is parallel to the c-axis, hence the A-site cation disorder has important implications for understanding the structural origins of the experimentally reported macroscopic polarization, as discussed further below.

The spontaneous polarization P_s for different configurations with fully relaxed tetragonal structure, calculated by both the Berry phase method and a point charge model, is shown in Figure 4c. While the point charge model implicitly only presumes purely ionic bonding, summing all the dipoles from polar displacements in the structure, the Berry phase method also takes electronic contributions into account[49]. The polarization calculated from the experimental structure[37] is included for comparison, and the range of literature values for the polarization of BKT [17, 20-25] is shown as a grey region. All configurations, except the layer-001, yield larger P_s than the range of experimental values. In contrast, the Berry phase calculated P_s for the experimental structure[37] is 30 μC/cm^2, which is well within the grey region depicting the range of reported values[17, 19, 23]. The analogue material BNT has a reported experimental polarization of 38 μC/cm^2 [50], and Berry phase calculations of P_s from a fully relaxed rhombohedral *R*3*c* unit cell structure gave a value of 62.6 μC/cm^2. However, when the experimental structure of BNT[50] is used as the basis for the Berry phase calculations a polarization P_s = 39.8 μC/cm^2 is obtained. The similar discrepancy between the calculated polarization for experimental and DFT relaxed structures for BKT and BNT strongly suggests that cation disorder is equally important to both materials and their solid solutions.

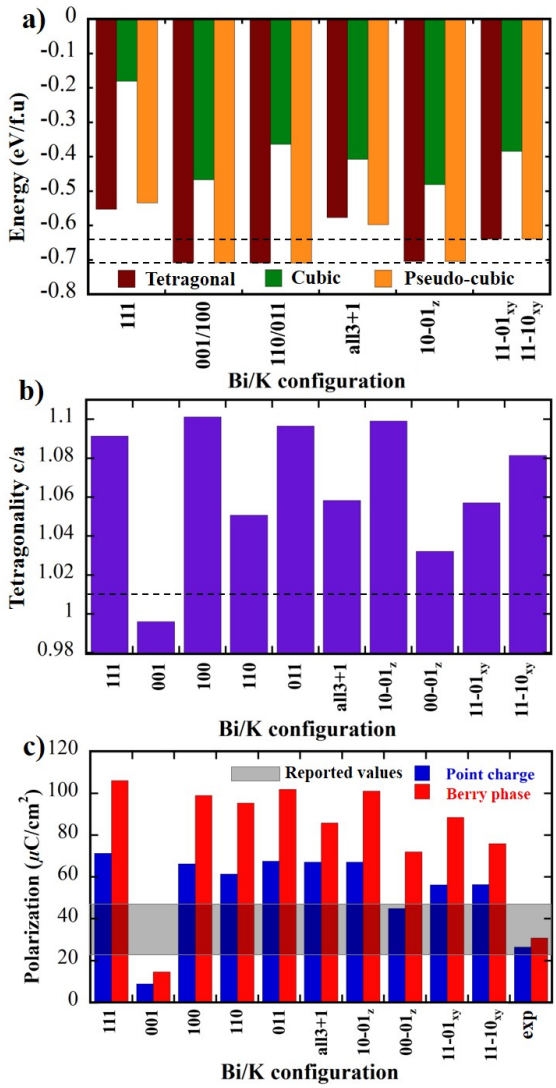

Figure 4: (a) Relative energy for fully relaxed tetragonal, cubic and pseudo-cubic structures of $Bi_{0.5}K_{0.5}TiO_3$. The zero energy level is set as the energy of 001 structure with tetragonal structure which has the highest energy. For comparison, we only give the lower value of the two configurations in 011/100, 110/011 and $11\text{-}01_{xy}$/$11\text{-}10_{xy}$ configurations with tetragonal structure. (b) Tetragonality c/a for fully relaxed tetragonal structures, the horizontal dashed line depicts the experimental value. (c) Polarization (P_s) of tetragonal structures from a point charge model (blue) and Berry phase calculations (red). The grey region represents experimentally reported values[17, 19, 23].

To further analyze the effect of cation disorder and displacements, we calculate the Born effective charges (BECs), denoted Z^*, which is defined as the change in polarization divided by the magnitude of the displacement of an ion[48, 49].

$$P = \frac{e}{\Omega}\sum_{j\beta} Z^*_{j\alpha\beta}\Delta u_{j\beta} \quad (1)$$

Here α is the displacement direction of atom j, and β is the polarization P in perpendicular directions. Equation (1) describes the contribution of an atom to the polarization (Z*-valence), and the total polarization can be obtained by the sum of all possible displacements of all sublattices. The BECs tend to be larger than their formal charges in displacive ferroelectrics[49]. Common effective charges for Bi^{3+}, K^+ and Ti^{4+} in ferroelectric oxides are about +5 for Bi^{3+}, +1.2 for K^+ and +7 for Ti^{4+} [51-53], respectively. In Table 1, we summarize the BECs of Bi^{3+}, K^+ and Ti^{4+} for different configurations in tetragonal BKT after full structural relaxation. We find that most of the effective charges for Z^*_{Ti4+} in Table 1 are smaller than the usual BECs, except in the layer-001 configuration and in the experimental structure. Combined with the c/a values shown in Figure 4b, we can infer that the polarization in BKT is not only dominated by the displacement of Ti, as in conventional displacive ferroelectrics like $PbTiO_3$ and $KNbO_3$, but also by the sum of all the local A-site cation configurations.

B. Experimental PDF modelling

To further study structural disorder in BKT we use the Pair Distribution Function (PDF) method to investigate the local and intermediate range structure. The experimental synchrotron X-ray PDF is first fitted to simple *P*4*mm* model (5 atoms) with 0.5 occupation of Bi and K on the A-site, corresponding to a random distribution of Bi and K on the A-site sublattice of BKT, see Figure 5a. The high r region above 12 Å probes the intermediate and average structure, while the low r regions correspond to the local structure. While the average structure for r > 12 Å can

be modelled with random A-site occupancy, the local structure for r < 12 Å is not well described by this model. Particularly the peaks at 3-3.5 Å, corresponding to Bi-Ti and K-Ti nearest-neighbor peaks, are not well reproduced by small-box modelling with random occupation, where Bi^{3+} and K^{+} are confined to the same positions. This indicates that the polar displacements of nearest-neighbor A- and B-site cations is strongly correlated due to local electrostatics. However, as the peaks at 3-3.5 Å are not reproduced in the model by including atomic correlated motion parameters (see Supplementary Information), we interpret this as a signature of strong structural disorder, even if the cation displacements are strongly correlated for nearest-neighbor A- and B-site cations. Random A-site occupation in a *P*4*mm* structure is thus not a realistic description of the local structure of BKT, nor are other space groups typically found in ferroelectric perovskites like *Amm*2, *R*3*m* or *R*3*c*. Extending the model to 2×2×2 supercells (40 atoms) with the ten different A-site cation configurations shown in Figure 2 does not substantially improve the fit to the local structure region, as the agreement factors for r = 1.5-6 Å summarized in Table 1 show.

As the small-box modelling described above inherently only considers long-range cation ordering, we performed large-box Reverse Monte Carlo (RMC) modelling of the PDF using a 12×12×12 supercell (8640 atoms). With this large number of atoms the finite width of the experimental G(r) peaks is modelled by a distribution of bond lengths instead of the thermal displacement factors used in small-box modelling, and this is discussed further below. With RMC large-box modelling we obtain an excellent fit for the whole r range of the PDF, as shown in Figure 5b. The cutoff at 24 Å reflects the finite size of the supercell model. To visualize the distribution of ionic positions the 12×12×12 *P*4*mm* supercell of BKT was folded into single unit cells in Figure 5c and 5d, where only Bi^{3+} and K^{+} cation "clouds" are shown for the A-site, respectively. The "clouds" of Bi^{3+}, K^{+}, Ti^{4+} and O^{2-} in BKT all show

spheroidal dispersive distributions. The "clouds" of O^{2-} are larger in part due to the lower X-ray scattering strength of O^{2-}. The results from large-box RMC modelling suggest a highly disordered structure, as visualized by the refined RMC supercell structure in Figure 5e).

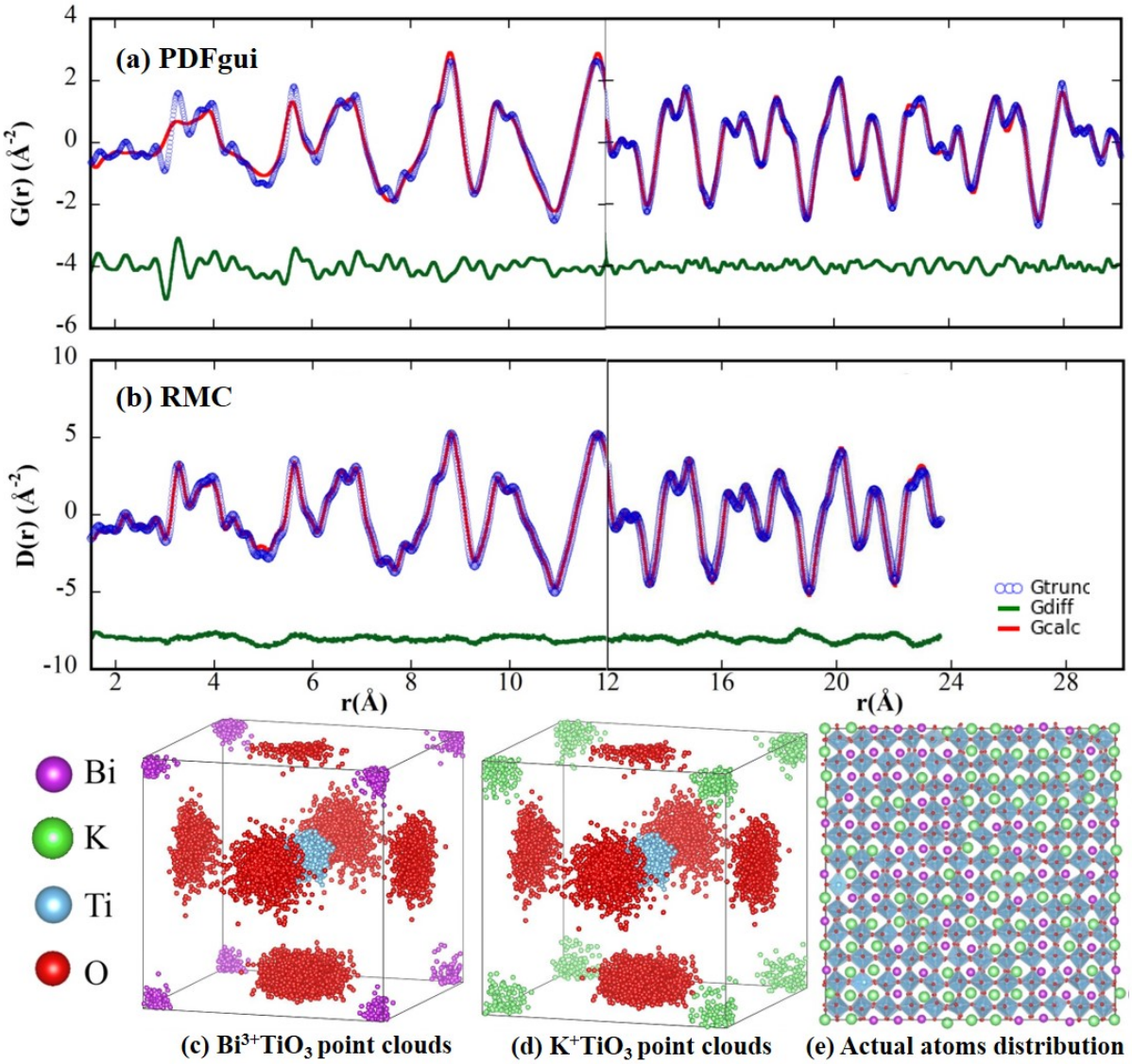

Figure 5: (a) PDF data of $Bi_{0.5}K_{0.5}TiO_3$ fitted with a *P*4*mm* random A-site occupancy small-box model (5 atoms). (b) Results of RMC simulation with a 12×12×12 *P*4*mm* supercell (8640 atoms), the cutoff at 24 Å reflects the finite size of the model. Open circles: experimental data; red solid lines: calculated data; green lines: difference curves. Folded RMC point "cloud" models only showing (c) Bi^{3+} and (d) K^+ cations on the A-site. e) RMC refined structure of the 12×12×12 supercell.

The folded RMC point clouds in Figure 5 c-e show the spatial distribution of all the atoms in the 12×12×12 supercell in a static picture. The finite width of the experimental G(r) peaks is influenced by both the thermal displacement factors of the atoms and the resolution with respect to beam, detector and the finite thickness of the diffracting volume of the sample. To illustrate the importance of these factors for RMC modelling we compare in Figure 6 our RMC results for mixed A-site $Bi_{0.5}K_{0.5}TiO_3$ with the prototypical multiferroic $BiFeO_3$ with long-range crystallographic order. The PDF pattern for $BiFeO_3$ was extracted from total scattering data collected with identical conditions as for BKT. The point clouds for the distribution of Bi^{3+} positions in $BiFeO_3$ in Figure 6b is significantly smaller than for Bi^{3+} in BKT in Figure 6a, reflecting the large degree of A-site disorder in BKT. Additionally, the BKT lattice is expanded compared to $BiFeO_3$ due to the larger size of the K^+ cation, and from a geometric perspective this allows for larger displacements of Bi^{3+} in BKT compared to $BiFeO_3$. Larger Bi^{3+} displacements caused by chemical pressure induced by K^+ is in analogy with enhanced local dipoles in $BaTiO_3$ nanoparticles where finite size effects lead to lattice expansion, which allows larger displacements of Ti^{4+} cations[56,57]. We also note that finite size effects in $BiFeO_3$ nanoparticles also cause strong disordering of the Bi^{3+} sublattice concomitant with lattice expansion[58,59]. The larger point clouds of Fe^{3+} compared to Bi^{3+} in $BiFeO_3$ is expected from Fe scattering X-rays more weakly than Bi. However, as Ti^{4+}, which is comparable to Fe^{3+} in terms of atomic number, shows only slightly larger point clouds in BKT than Fe^{3+} does in $BiFeO_3$, we can infer that the structural disorder on the A-site sublattice of BKT does not cause a comparable degree of disorder in the B-site sublattice. The size of the point clouds from RMC modelling are comparable to the size of the U_{iso} displacement ellipsoids from Rietveld refinement, see Table S1 in the Supplementary Information.

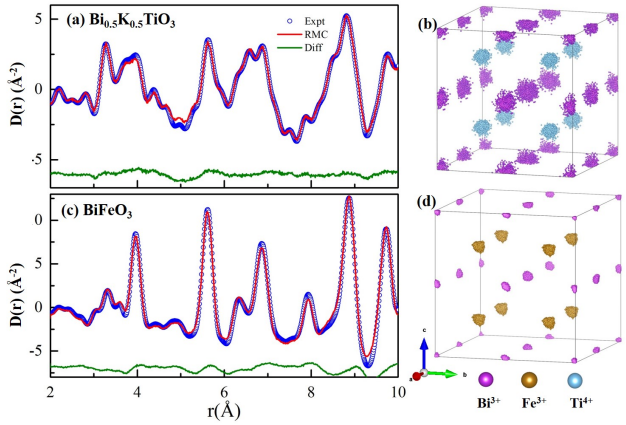

Figure 6: Comparison of RMC modelling of experimental PDFs of $Bi_{0.5}K_{0.5}TiO_3$ and $BiFeO_3$. (a) RMC fitting of a PDF for $Bi_{0.5}K_{0.5}TiO_3$ with (b) folded RMC point clouds showing only Bi^{3+} and Ti^{4+} cations. (c) RMC simulation of a PDF of $BiFeO_3$ with folded RMC point clouds showing only Bi^{3+} and Fe^{3+} cations.

Having established that BKT displays strong A-site disorder we now turn our attention to the intermediate range structure. Although the average *P4mm* structure with random A-site occupation does not give a good fit for the low-r region, modelling the experimental G(r) for different r-ranges can still provide information about the intermediate range and long range structural coherence. Fitting the G(r) from r_{min} = 1.5 Å to a varying r_{max} from 80 to 10 Å yields the r-range dependent lattice parameters, tetragonality c/a and Ti^{4+} displacement shown in Figure 7. With decreasing r_{max} the refined lattice parameter c increases significantly while the lattice parameter a decreases subtly (Figure 7a), resulting in an overall increase of the c/a ratio (Figure 7b) as we go from probing the intermediate range structure to the local structure. From r_{max} = 25 Å the fits become worse with oscillating refined values for the lattice parameters, indicating a structural coherence length of 25 Å or less. Reducing r_{max} from r_{max} = 16 Å, corresponding to 4 perovskite unit cells gives a rapid increase in the c/a ratio. This suggests that the local structure is more strained than the average structure, where local lattice strains in different directions, depending on the local A-site cation configuration, are averaged out. The

large refined tetragonal strain on the local scale with low r_{max} is consistent with the large c/a ratios of the DFT relaxed tetragonal structures shown in Figure 4b. This is further supported by the evolution of the Ti^{4+} displacement with r_{max}; while being close to constant for high r_{max} values, below 20 Å the refinements yield larger displacements, albeit with larger uncertainties as the fitted r-range becomes smaller. This is qualitatively in agreement with the DFT calculations presented in section A where the calculated polarization for all cation configurations, except the 001, is significantly larger than the experimental range of values. If one specific cation configuration is only repeated for 4-5 unit cells or less, the local structure giving rise to a large polarization in one direction is replaced by a different cation configuration in a neighboring region, with partly cancelling local polarization.

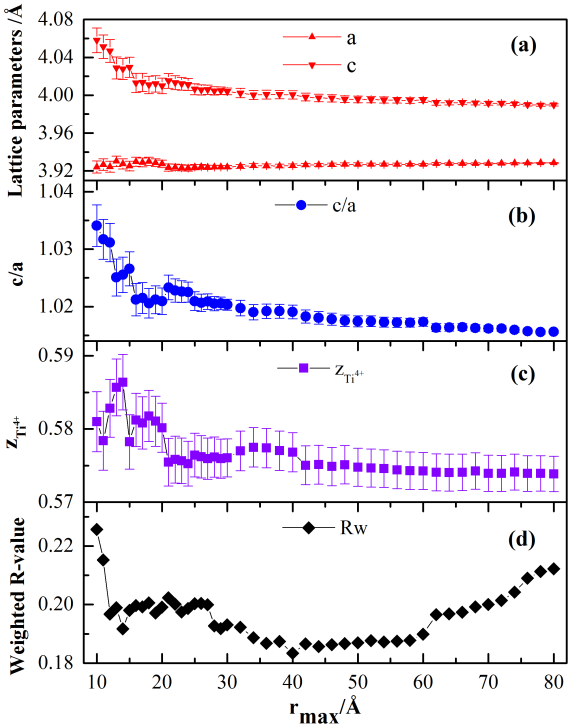

Figure 7: Evolution of the (a) lattice parameters, (b) tetragonality c/a, (c) Ti^{4+} displacements and (d) The weighted R-value (Rw) factors with varying r_{max} for fitting the G(r) of $Bi_{0.5}K_{0.5}TiO_3$ with the average *P*4*mm* structure with random A-site occupation. The r_{min} was fixed to 1.5Å while the r_{max} was varied from 80Å to 10Å. The scale factor and Q_{damp} was fixed to the value

refined for r_{max} = 80 Å for all other values of r_{max}.

C. A model for a disordered ferroelectric

To correlate structural disorder and ferroelectric polarization we now combine RMC simulations and DFT calculations to construct a disordered average structural model for BKT. As a structure model with 8640 atoms is unfeasible for DFT calculations, we perform RMC modelling of the G(r) with a 4×4×4 supercell containing 320 atoms, $Bi_{32}K_{32}Ti_{64}O_{192}$, and the refined structure is shown in Figure 8a. As oxygen is a weak X-ray scatterer, the uncertainty of the refined positions of the O^{2-} anions is significant. To mitigate this uncertainty, we use the refined RMC model in Figure 8a as the input structure for DFT calculations and relax the ion positions to arrive at a disordered structural model with realistic O^{2-} positions. The DFT relaxed structure depicted in Figure 8b displays less distorted $TiO_{6/2}$ octahedra and smaller polar displacements of Bi and K along the z-direction with respect to the TiO-sublattice due to the optimized chemical bonds. The PDF simulated by RMC for this smaller supercell model still reproduces the experimental G(r) well, as shown in Figure 8c, but with more noise due to the smaller number of possible bond lengths.

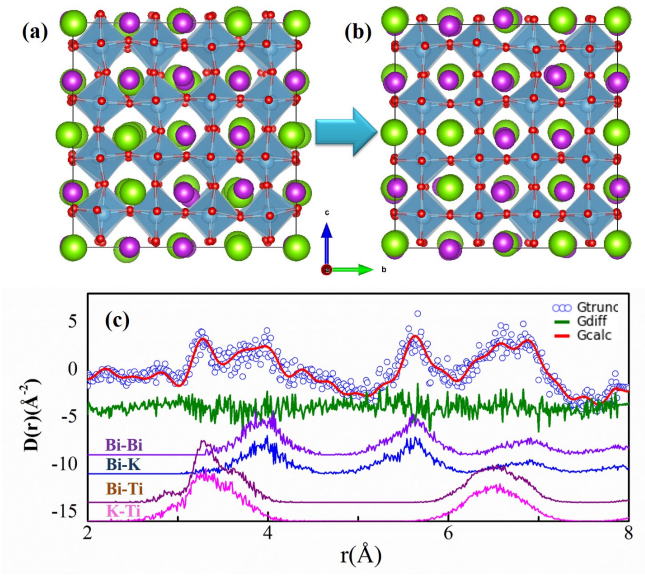

Figure 8: (a) Initial 4×4×4 supercell model from RMC fitting of the experimental G(r) for $Bi_{0.5}K_{0.5}TiO_3$. (b) Final structure after geometry optimization by DFT of the model in (a), with spontaneous polarization $P_{s,z}$=29μC/cm^2, $P_{s,x}$= 6μC/cm^2, $P_{s,y}$=10μC/cm^2 from point charge calculations. (c) Experimental G(r) and RMC simulation with a 4×4×4 supercell, with partial PDFs derived from the RMC modelled 12×12×12 supercell in Figure 5 shown below.

The spontaneous polarization P_s of the structural model of BKT in Figure 9b obtained from a point charge method is $P_{s,z}$=29μC/cm^2, $P_{s,x}$= 6μC/cm^2, $P_{s,y}$=10μC/cm^2 , giving a vector sum of P_s = 31μC/cm^2, which is well within the range of reported experimental values, and very close to the Berry phase calculated polarization (Figure 4c) of the average *P*4*mm* structure[37]. Although the point charge model derived polarization is always smaller than the Berry phase calculated, due to neglect of the electronic contribution, it is still a strong indication of the spontaneous polarization, as seen in Figure 4c. A disordered structure without long-range ordering of Bi^{3+} and K^+ is thus a more realistic model for the structure of BKT than the *P*4*mm* structure with random A-site occupation, which Figure 7 shows is the spatially averaged structure. The Bi-Ti partial PDF peak around 3.5 Å, inferred from RMC modelling, is both broad and asymmetric, as shown in Figure 8c. The broad peak implies a distribution of bond lengths, and with it a continuous disorder rather than discrete disorder, and this cannot be well described by an average mixed A-site *P*4*mm* model, as illustrated Figure 5a.

The bond length distributions for the coordination polyhedra TiO_6 and $(Bi/K)O_{12}$ from different tetragonal A-site configurations with full DFT optimization are shown in Figure 9a. After geometry optimization, the Bi-O and K-O bonds show two distinctly different bond length distributions because of their different formal charges and preferred local environments, as also

reported for BNT[8, 54, 55]. The distribution of all Bi-O bond lengths show three different regions, in agreement with the peaks of a Bi-O partial PDF extracted from the RMC fitting. In contrast, the K-O bond length distribution does not display distinctly different regions. The different formal charges and bond lengths towards oxygen for Bi^{3+} and K^{+} cause a relative shift between Bi^{3+} and K^{+} along the c-axis, as illustrated in Figure 9b, enhancing the c/a ratio and the local polarization. The Ti-O bond length distribution is more narrow than for the A-site dodecahedra, reflecting the smaller size and more rigid nature of the $TiO_{6/2}$ octahedra.

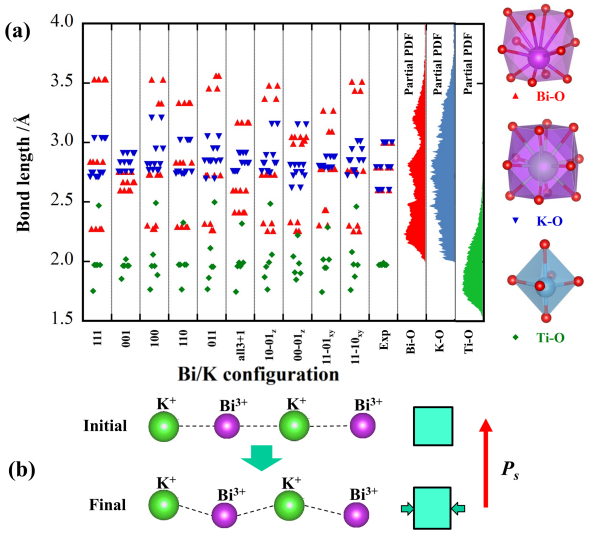

Figure 9: (a) Bond length distributions for the A- and B-site polyhedra in $Bi_{0.5}K_{0.5}TiO_3$ for the different A-site configurations after geometry optimization by DFT, the mixed A-site structure derived from small-box modelling (labelled Exp), and the Bi-O, K-O and Ti-O bonds lengths from RMC modelling. (b) Excerpts showing the relative shift between Bi^{3+} and K^{+} along the c-axis after geometry optimization by DFT.

Based on the presented DFT and PDF analysis, BKT displays A-site disorder and the disordered structure model also gives a calculated spontaneous polarization similar to the experimental values, as seen in Figure 4c. In an ordered structure, the local polarization vectors all add up and contribute to the experimentally observed polarization. In contrast, different local A-site

configurations in a disordered structure co-exist and partly cancel each other. The local cation configuration, determined during synthesis or sintering at high temperature, governs the direction of the local polarization after cooling the material below the Curie temperature. The discrepancy between the experimentally reported polarization values and the DFT calculated values for ordered cation configurations in Figure 4c follows naturally from this interpretation. The reported relaxor behaviour of BKT is also consistent with our structural model, as local polar regions are expected to respond differently to an AC electric field, with diffuse, frequency-dependent permittivity maxima characteristic to ferroelectric relaxors[4,29]. A larger-scale illustration of the disordered structure of BKT is given in Figure 10 where each cube represents a 2×2×2 supercell and the arrows the local polarization vectors. The net absolute polarization decreases when probing an increasing volume of material, as illustrated in the embedded trend chart.

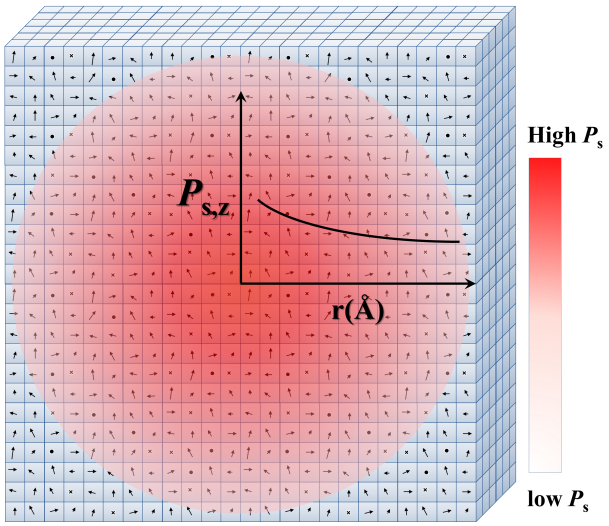

Figure 10: Proposed 3D microstructure model of $Bi_{0.5}K_{0.5}TiO_3$. The embedded trend chart illustrates how the net absolute polarization decreases when probing an increasing volume of material.

IV. CONCLUSIONS

In summary, the local structure and cation disorder in A-site BKT was investigated by DFT calculations and PDF extracted from synchrotron X-ray total scattering. No simple Bi/K cation configuration could be identified as the most stable from DFT, and the polarization calculated for long-range cation order is higher than the experimentally reported. The calculated Born effective charges show that the polarization is not only dominated by the displacement of Ti^{4+}, like in a displacive ferroelectric, but also by the unit cell distortion caused by the local A-site cation ordering. Bond length analysis shows distinctly different local environments for Bi and K. Small-box and large-box modelling of the experimental PDF support a A-site disordered structural model, and the structural coherence inferred from PDF shows distinct anomalies at 25 Å and 16 Å length scales. A disordered 4×4×4 supercell model was constructed to fit the experimental PDF and the spontaneous polarization calculated for this model agrees with experimental values.

Supporting Information

Additional results from Rietveld refinements and small-box refinements of pair distribution functions (PDF), and more details on the treatment of correlated atomic motion in PDFs.

ACKNOWLEDGMENTS

This work was supported by the Research Council of Norway through the SYNKNØYT project 228571/F50. Computational resources were provided by the Norwegian Metacenter for Computational Science (NOTUR) through the project NN9264K. We thank Andrew Fitch for his valuable assistance at beamline ID22 at ESRF.

References

(1) Rödel, J.; Jo, W.; Seifert, K. T. P.; Anton, E. M.; Granzow, T.; Damjanovic, D., Perspective on the development of lead-free piezoceramics. *J. Am. Ceram. Soc.* **2009,** *92*, 1153-1177.

(2) Shvartsman, V. V.; Lupascu, D. C., Lead-Free Relaxor Ferroelectrics. *J. Am. Ceram. Soc.* **2012,** *95*, 1-26.

(3) Hou, Y. D.; Hou, L.; Yang, J. F.; Zhu, M. K.; Wang, H.; Yan, H., Comparative study of formation mechanism of $K_{0.5}Bi_{0.5}TiO_3$ powders synthesized by three chemical methods. *Acta Chim. Sinica* **2007,** *65*, 950-954.

(4) Yang, J. F.; Hou, Y. D.; Wang, C.; Zhu, M. K.; Yan, H., Relaxor behavior of $(K_{0.5}Bi_{0.5})TiO_3$ ceramics derived from molten salt synthesized single-crystalline nanowires. *Appl. Phys. Lett.* **2007,** *91*, 023118.

(5) Konig, J.; Spreitzer, M.; Jancar, B.; Suvorov, D.; Samardzija, Z.; Popovic, A., The thermal decomposition of $K_{0.5}Bi_{0.5}TiO_3$ ceramics. *J. Eur. Ceram. Soc.* **2009,** *29*, 1695-1701.

(6) Rao, P. V. B.; Ramana, E. V.; Sankaram, T. B., Electrical properties of $K_{0.5}Bi_{0.5}TiO_3$. *J. Alloys Compd.* **2009,** *467*, 293-298.

(7) Krad, I.; Bidault, O.; Geoffroy, N.; Maaoui, M. E. L., Preparation and characterization of $K_{0.5}Bi_{0.5}TiO_3$ particles synthesized by a stirring hydrothermal method. *Ceram. Int.* **2016,** *42*, 3751-3756.

(8) Aksel, E.; Forrester, J. S.; Nino, J. C.; Page, K.; Shoemaker, D. P.; Jones, J. L., Local atomic structure deviation from average structure of $Na_{0.5}Bi_{0.5}TiO_3$: Combined x-ray and neutron total scattering study. *Phys. Rev. B* **2013,** *87*, 104113.

(9) Rao, B. N.; Datta, R.; Chandrashekaran, S. S.; Mishra, D. K.; Sathe, V.; Senyshyn, A.; Ranjan, R., Local structural disorder and its influence on the average global structure and polar properties in $Na_{0.5}Bi_{0.5}TiO_3$. *Phys. Rev. B* **2013,** *88*, 224103.

(10) Gröting, M.; Hayn, S.; Albe, K., Chemical order and local structure of the lead-free relaxor ferroelectric. *J. Solid State Chem.* **2011,** *184*, 2041-2046.

(11) Gröting, M.; Albe, K., Comparative study of A-site order in the lead-free bismuth titanates $M_{1/2}Bi_{1/2}TiO_3$ (M=Li, Na, K, Rb, Cs, Ag, Tl) from first-principles. *J. Solid State Chem.* **2014,** *213*, 138-144.

(12) Wefring, E. T.; Morozov, M. I.; Einarsrud, M.-A.; Grande, T.; Trolier-McKinstry, S. E., Solid-State Synthesis and Properties of Relaxor (1−x)BKT-xBNZ Ceramics. *J. Am. Ceram. Soc.* **2014,** *97*, 2928-2935.

(13) Smolenskii, G. A.; Isupov, V. A.; Agranovskaya, A. I.; Krainik, N. N., New ferroelectrics of a complex composition: 4. *Soviet Physics-Solid State* **1961,** *2*, 2651-2654.

(14) Zhao, S. C.; Li, G. R.; Ding, A. L.; Wang, T. B.; Yin, Q. R., Ferroelectric and piezoelectric properties of $(Na, K)_{0.5}Bi_{0.5}TiO_3$ lead free ceramics. *J. Phys. D Appl. Phys.* **2006,** *39*, 2277-2281.

(15) Shuvaeva, V. A.; Zekria, D.; Glazer, A. M.; Jiang, Q.; Weber, S. M.; Bhattacharya, P.; Thomas, P. A., Local structure of the lead-free relaxor ferroelectric$(K_xNa_{1-x})_{0.5}Bi_{0.5}TiO_3$. *Phys. Rev. B* **2005,** *71*, 174114.

(16) Levin, I.; Reaney, I. M.; Anton, E. M.; Jo, W.; Rödel, J.; Pokorny, J.; Schmitt, L. A.; Kleebe, H. J.; Hinterstein, M.; Jones, J. L., Local structure, pseudosymmetry, and phase transitions in $Na_{1/2}Bi_{1/2}TiO_3$–$K_{1/2}Bi_{1/2}TiO_3$ ceramics. *Phys. Rev. B* **2013,** *87*, 024113.

(17) Hiruma, Y.; Aoyagi, R.; Nagata, H.; Takenaka, T., Ferroelectric and Piezoelectric Properties of $(Bi_{1/2}K_{1/2})TiO_3$ Ceramics. *Jpn. J. Appl. Phys.* **2005,** *44*, 5040-5044.

(18) Wefring, E. T.; Schader, F. H.; Webber, K. G.; Einarsrud, M. A.; Grande, T., Electrical conductivity and ferroelastic properties of Ti-substituted solid solutions (1-x)$BiFeO_3$ - x$Bi_{0.5}K_{0.5}TiO_3$. *J. Eur. Ceram. Soc.* **2016,** *36*, 497-506.
(19) Hiruma, Y.; Nagata, H.; Takenaka, T., Grain-size effect on electrical properties of $(Bi_{1/2}K_{1/2})TiO_3$ ceramics. *Jpn. J. Appl. Phys.* **2007,** *46*, 1081-1084.
(20) Tabuchi, K.; Inoue, Y.; Nagata, H.; Takenaka, T., Effects of starting raw materials for fabricating dense $(Bi_{1/2}K_{1/2})TiO_3$ ceramics. *Ferroelectrics* **2013,** *457*, 124-130.
(21) Rao, P. V. B.; Sankaram, T. B., Impedance spectroscopy studies of $K_{0.5}Bi_{0.5}TiO_3$. *J. Electroceram.* **2010,** *25*, 60-69.
(22) Hagiwara, M.; Fujihara, S., Grain size effect on phase transition behavior and electrical properties of $(Bi_{1/2}K_{1/2})TiO_3$ piezoelectric ceramics. *Jpn. J. Appl. Phys.* **2015,** *54*, 10ND10.
(23) Konig, J.; Suvorov, D., Evolution of the electrical properties of $K_{0.5}Bi_{0.5}TiO_3$ as a result of prolonged sintering. *J. Eur. Ceram. Soc.* **2015,** *35*, 2791-2799.
(24) Hiruma, Y.; Marumo, K.; Aoyagi, R.; Nagata, H.; Takenaka, T., Ferroelectric and piezoelectric properties of $(Bi_{1/2}K_{1/2})TiO_3$ ceramics fabricated by hot-pressing method. *J. Electroceram.* **2008,** *21*, 296-299.
(25) Suchanicz, J.; Roleder, K.; Kania, A.; Handerek, J., Electrostrictive strain and pyroeffect in the region of phase coexistence in $Na_{0.5}Bi_{0.5}TiO_3$. *Ferroelectrics* **1988,** *77*, 107-110.
(26) Ivanova, V. V., Kapyshev, A.G., Venevtsev, Yu.N., Zhdanov, G.S., X-ray determination of the symmetry of the ferroelectric compounds (potassium or sodium) (0.5) bismuthi (0.5) titanate and the high temperature phase transitions in potassium (0.5) bismuth (0.5) titanate. *Bull. Acad. Sci. USSR Phys. Ser.* **1962,** *26*, 358-360.
(27) Burns, G.; Dacol, F. H., Glassy polarisation behaviour in ferroelectric compounds $Pb(Mg_{1/3}Nb_{2/3})O_3$ and $Pb(Zn_{1/3}Nb_{2/3})O_3$. *Solid State Commun.* **1983,** *48*, 853-856.
(28) Otonicar, M.; Skapin, S. D.; Jancar, B.; Ubic, R.; Suvorov, D., Analysis of the phase transition and the domain structure in $K_{0.5}Bi_{0.5}TiO_3$ perovskite ceramics by in situ XRD and TEM. *J. Am. Ceram. Soc.* **2010,** *93*, 4168-4173.
(29) Hagiwara, M.; Fujihara, S., Grain-size-dependent spontaneous relaxor-to-ferroelectric phase transition in $(Bi_{1/2}K_{1/2})TiO_3$ ceramics. *Appl. Phys. Lett.* **2015,** *107*, 012903.
(30) Ozaki, T.; Matsuo, H.; Noguchi, Y.; Miyayama, M.; Mori, S., Microstructures Related to Ferroelectric Properties in $(Bi_{0.5}K_{0.5})TiO_3$–$BiFeO_3$. *Jpn. J. Appl. Phys.* **2010,** *49*, 09MC05.
(31) Kim, J. M.; Sung, Y. S.; Cho, J. H.; Song, T. K.; Kim, M. H.; Chong, H. H.; Park, T. G.; Do, D.; Kim, S. S., Piezoelectric and Dielectric Properties of Lead-Free (1-x)$(Bi_{0.5}K_{0.5})TiO_3$-x$BiFeO_3$ Ceramics. *Ferroelectrics* **2010,** *404*, 88-92.
(32) Matsuo, H.; Noguchi, Y.; Miyayama, M.; Suzuki, M.; Watanabe, A.; Sasabe, S.; Ozaki, T.; Mori, S.; Torii, S.; Kamiyama, T., Structural and piezoelectric properties of high-density $(Bi_{0.5}K_{0.5})TiO_3$–$BiFeO_3$ ceramics. *J. Appl. Phys.* **2010,** *108*, 104103.
(33) Morozov, M. I.; Einarsrud, M. A.; Grande, T.; Damjanovic, D., Lead-Free Relaxor-Like $0.75Bi_{0.5}K_{0.5}TiO_3$–$0.25BiFeO_3$ Ceramics with Large Electric Field-Induced Strain. *Ferroelectrics* **2012,** *439*, 88-94.
(34) Morozov, M. I.; Einarsrud, M.-A.; Grande, T., Polarization and strain response in $Bi_{0.5}K_{0.5}TiO_3$-$BiFeO_3$ ceramics. *Appl. Phys. Lett.* **2012,** *101*, 252904.
(35) Morozov, M. I.; Einarsrud, M.-A.; Grande, T., Atmosphere controlled conductivity and Maxwell-Wagner relaxation in $Bi_{0.5}K_{0.5}TiO_3$-$BiFeO_3$ ceramics. *J. Appl. Phys.* **2014,** *115*, 044104.
(36) King, G.; Woodward, P. M., Cation ordering in perovskites. *J. Mater. Chem.* **2010,** *20*, 5785.
(37) Jones, G. O.; Kreisel, J.; Thomas, P. A., A structural study of the $(Na_{1-x}K_x)_{0.5}Bi_{0.5}TiO_3$ perovskite series as a function of substitution (x) and temperature. *Powder Diffr.* **2002,** *17*, 301-319.

(38) Selbach, S. M; Tybell, T.; Einarsrud, M.-A.; Grande, T., High-temperature semiconducting cubic phase of $BiFe_{0.7}Mn_{0.3}O_{3+\delta}$. *Phys. Rev. B* **2009,** *79*, 214113.
(39) Larson, A. C.; Dreele, R. B. V., General Structure Analysis System technical manual. *LANSCE, MS–H805 Los Almos National Laboratory LAUR* **2000**, 86-748.
(40) Toby, B. H., EXPGUI, a graphical user interface for GSAS. *J. Appl. Crystallogr.* **2001,** *34*, 210-213.
(41) Juhas, P.; Davis, T.; Farrow, C. L.; Billinge, S. J. L., PDFgetX3: a rapid and highly automatable program for processing powder diffraction data into total scattering pair distribution functions. *J. Appl. Crystallogr.* **2013,** *46*, 560-566.
(42) Farrow, C. L.; Juhas, P.; Liu, J. W.; Bryndin, D.; Bozin, E. S.; Bloch, J.; Proffen, T.; Billinge, S. J., PDFfit2 and PDFgui: computer programs for studying nanostructure in crystals. *J. Phys. Condens. Matter* **2007,** *19*, 335219.
(43) Tucker, M. G.; Keen, D. A.; Dove, M. T.; Goodwin, A. L.; Hui, Q., RMCProfile: reverse Monte Carlo for polycrystalline materials. *J. Phys. Condens. Matter* **2007,** *19*, 335218.
(44) Kresse, G.; Furthmuller, J., Efficient iterative schemes for ab initio total-energy calculations using a plane-wave basis set. *Phys. Rev. B* **1996,** *54*, 11169-11186.
(45) Kresse, G.; Joubert, D., From ultrasoft pseudopotentials to the projector augmented-wave method. *Phys. Rev. B* **1999,** *59*, 1758-1775.
(46) Perdew, J. P.; Ruzsinszky, A.; Csonka, G. I.; Vydrov, O. A.; Scuseria, G. E.; Constantin, L. A.; Zhou, X. L.; Burke, K., Restoring the density-gradient expansion for exchange in solids and surfaces. *Phys. Rev. Lett.* **2008,** *100*, 136406.
(47) Perdew, J. P.; Burke, K.; Ernzerhof, M., Generalized gradient approximation made simple. *Phys. Rev. Lett.* **1996,** *77*, 3865-3868.
(48) Kingsmith, R. D.; Vanderbilt, D., Theory of polarization of crystalline solids. *Phys. Rev. B* **1993,** *47*, 1651-1654.
(49) Spaldin, N. A., A beginner's guide to the modern theory of polarization. *J. Solid State Chem.* **2012,** *195*, 2-10.
(50) Niranjan, M. K.; Karthik, T.; Asthana, S.; Pan, J.; Waghmare, U. V., Theoretical and experimental investigation of Raman modes, ferroelectric nd dielectric properties of relaxor $Na_{0.5}Bi_{0.5}TiO_3$. *J. Appl. Phys.* **2013,** *113*, 194106.
(51) Roy, A.; Prasad, R.; Auluck, S.; Garg, A., First-principles calculations of Born effective charges and spontaneous polarization of ferroelectric bismuth titanate. *J. Phys. Condens. Matter* **2010,** *22*, 165902.
(52) Wan, L. F.; Nishimatsu, T.; Beckman, S. P., The structural, dielectric, elastic, and piezoelectric properties of $KNbO_3$ from first-principles methods. *J. Appl. Phys.* **2012,** *111*, 104107.
(53) Ghosez, P.; Michenaud, J. P.; Gonze, X., Dynamical atomic charges: The case of ABO_3 compounds. *Phys. Rev. B* **1998,** *58*, 6224-6240.
(54) Jeong, I.; Park, C. Y.; Kim, D. J.; Kim, S. H.; Moon, B. K.; Kim, W.; Ahn, C. W., Neutron total scattering studies on A-site disorder in lead-free ferroelectric $Bi_{0.5}(Na_{1-x}K_x)_{0.5}TiO_3$. *Z. Kristallogr.* **2011,** *226*, 150-154.
(55) Keeble, D. S.; Barney, E. R.; Keen, D. A.; Tucker, M. G.; Kreisel, J.; Thomas, P. A., Bifurcated Polarization Rotation in Bismuth-Based Piezoelectrics. *Adv. Funct. Mater.* **2013,** *23*, 185-190.
(56) Smith, M. N.; Page, K.; Siegrist, T.; Redmond, P. L., Walter, W. C.; Seshadri, R.; Brus, L. E; Steigerwald, M. L., Crystal Structure and the Paraelectric-to-Ferroelectric Phase Transition of Nanoscale $BaTiO_3$. *J. Am. Chem. Soc.*, **2008**, *130*, 6955-6963.
(57) Page, K.; Proffen, T.; Niederberger, M.; Seshadri, R., Probing Local Dipoles and Ligand Structure in $BaTiO_3$ Nanoparticles. *Chem. Mater.*, **2010**, *22*, 4386-4391.
(58) Petkov, V.; Selbach, S. M.; Einarsrud, M.-A.; Grande, T.; Shastri, S. D., Melting of Bi

Sublattice in Nanosized $BiFeO_3$ Perovskite by Resonant X-Ray Diffraction. *Phys. Rev. Lett.*, **2010**, *105*, 185501.
(59) Selbach, S. M.; Tybell, T.; Einarsrud, M.-A.; Grande T., Size-Dependent Properties of Multiferroic $BiFeO_3$ Nanoparticles, *Chem. Mater.*, **2007**, *19*, 6478-6484.

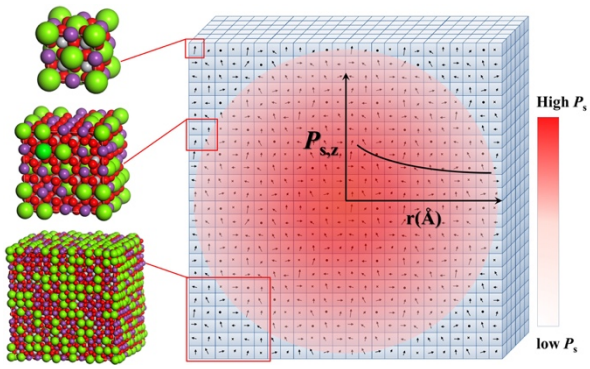

Local structural disorder in lead-free ferroelectric $Bi_{0.5}K_{0.5}TiO_3$ is analyzed by pair distribution functions (PDF) and density functional theory (DFT) calculations.